Renewable Energy 245 (2025) 122822

Contents lists available at ScienceDirect

Renewable Energy

journal homepage: www.elsevier.com/locate/renene

Experimental analysis of graphene-COOH/water and TiO_2/Water nanofluids in plate heat exchangers: Heat transfer performance and stability

Saeed Zeinali Heris [a,b,*], Siavash Pasvei [b], Hadi Pourpasha [a], Yaghoub Mohammadfam [a], Mohsen Sharifpur [c,d,**], Josua Meyer [e]

[a] School of Safety Science and Engineering, Xi'an University of Science and Technology, No.58, Middle Section of Yanta Road, Xi'an, Shaanxi, 710054, China
[b] Faculty of Chemical and Petroleum Engineering, University of Tabriz, Tabriz, Iran
[c] School of Mechanical, Industrial and Aeronautical Engineering, University of the Witwatersrand, Private Bag 3, Wits, 2050, South Africa
[d] Department of Medical Research, China Medical University Hospital, China Medical University, Taichung, Taiwan
[e] Department of Mechanical and Mechatronics Engineering, Stellenbosch University, Stellenbosch, 7602, South Africa

ARTICLE INFO

Keywords:
Energy efficiency improvement
Plate heat exchangers
TiO_2/Water and graphene-COOH/Water nanofluids
Heat transfer enhancement

ABSTRACT

This study investigates the thermal performance of nanofluids (NFs) in plate heat exchangers (PHEXs), focusing on graphene-COOH/water and TiO_2/water NFs as working fluids. The attributes of nanofluids, such as thermal conductivity (TC), specific heat capacity (SHC), viscosity, and density, were measured using the KD2 pro thermal analyzer, Cannon-Fenske opaque viscometer, and a density meter, which is a distinguishing aspect of this study. The maximum TC value is associated with the graphene-COOH/water nanofluid at 0.05 wt%, showing a 29.6 % increase compared to water. The convection heat transfer coefficient (CHTC) was also notably improved, with graphene-COOH/water achieving a 27.8 % enhancement compared to 15.6 % for TiO_2/water. Furthermore, the study reveals that increasing the mass fraction of nanoparticles (NPs) results in a slight increase in pressure drop (ΔP), with a maximum increase of 3.8 % compared to water, which is considered negligible. The graphene-COOH/water NF demonstrated the highest performance index (η) of 1.247 at a Reynolds number of 134.59, indicating a 24.7 % improvement in efficiency. Overall, the findings suggest that the incorporation of NFs, particularly graphene-COOH/water, can significantly enhance the thermal efficiency of PHEXs while maintaining manageable ΔP, making them a promising option for industrial applications.

Nomenclature

A	Heat transfer surface (m^2)
b	Depth of plates (mm)
Ag	Silver
C_p	Specific heat capacity (J/kg.K)
CF	Cold fluid
CHTC	Convection heat transfer coefficient
d	diameter
D_p	Diameter of ducts
F	Correction factor of the plate heat exchanger
f	Friction coefficient
FTIR	Fourier-transform infrared
h	Convection heat transfer coefficient ($W/m^2.K$)

(*continued on next column*)

(*continued*)

HEXs	Heat exchangers
HF	Hot fluid
HTR	Heat transfer rate
k	Thermal conductivity coefficient (W/m.K)
Re	Reynolds number
L	Length (m)
m	Mass (kg)
$\dot{m}$	mass flow rate (kg/s)
N	Number of plates
NF	Nanofluid
NP	Nanoparticle
Nu	Nusselt number
OHTC	Overall heat transfer coefficient

(*continued on next page*)

* Corresponding author. Xi'an University of Science and Technology, No.58, Middle Section of Yanta Road, Xi'an, Shaanxi, 710054, China.
** Corresponding author. School of Mechanical, Industrial and Aeronautical Engineering, University of the Witwatersrand, Private Bag 3, Wits 2050, South Africa.
E-mail addresses: sz.heris@xust.edu.cn (S. Zeinali Heris), hadipourpasha@gmail.com (H. Pourpasha), y_mohammadfam89@yahoo.com (Y. Mohammadfam), mohsen.sharifpur@wits.ac.za (M. Sharifpur).

https://doi.org/10.1016/j.renene.2025.122822
Received 13 November 2024; Received in revised form 1 February 2025; Accepted 5 March 2025
Available online 7 March 2025

(*continued*)

Pe	Peclet number
P_c	Corrugation pitch (mm)
PHEXs	Plate heat exchangers
Pr	Prandtl number
ΔP	Pressure drop (Pa)
Q	absorbed or dissipated heat (W)
RE	Ratio
SEM	Scanning electron microscopy
SHC	Specific heat capacity
T	Temperature (°C)
THP	Thermal performance
ΔT_{LMTD}	Average logarithmic temperature
U	Overall heat transfer coefficient ($W/m^2.K$)
u_n	Fluid bulk velocity (m/s)
U_{Ri}	Maximum possible error
Uxi	Measurement error
$\dot{V}$	Volume flow rate (L/min)
w	Width of plates (mm)
wt	weight
x_i	Measurable parameter
XRD	X-ray diffraction
Greek letters	
ε	Efficiency of PHEX
φ	Nanoparticle mass fraction (wt.%)
ϕ	Nanoparticle volume fraction (vol%)
ρ	Density (kg/m^3)
μ	Dynamic viscosity (Pa.s)
γ	Aspect ratio of the PHEX channels
β	Angle along of plates
χ	Surface increase ratio
Subscripts	
ave	Average
bf	Base fluid
d	Diagonal
c	Cold fluid
h	Hot fluid
hy	hydraulic
i	Inlet
LMTD	logarithmic mean temperature difference
nf	Nanofluid
mt	Total mass
o	Outlet
P	Nanoparticle
W	Water

1. Introduction

Heat exchangers (HEXs) are fundamental devices used in numerous industries and applications to transfer thermal energy between multiple fluids while ensuring their separation. These essential devices are instrumental in optimizing energy consumption, enhancing efficiency, and maintaining optimal operating conditions across diverse processes [1]. By harnessing the principles of heat transfer, HEXs facilitate the exchange of heat from a hot fluid (HF) to a colder one, enabling heat recovery, temperature control, and thermal management in a wide range of systems [2,3]. The primary objective of a HEX is to optimize the heat transfer rate (HTR) while minimizing ΔP and energy losses. This is achieved through careful design considerations, including the selecting of appropriate heat transfer surfaces, optimizing of fluid flow patterns, and the choice of suitable materials that can withstand the operating conditions and resist fouling or corrosion [4,5].

HEXs are classified by design, flow configuration, and heat transfer mechanisms. Common types include finned-tube, shell-and-tube, plate heat exchangers (PHEXs), and double-pipe HEXs, each serving specific applications [6,7]. PHEXs are indirect-contact systems made of thin, corrugated metal plates with holes for fluid flow, enhancing heat exchange. These plates are assembled with gaskets or welds to seal flow channels. The design promotes turbulence, improving heat transfer efficiency. PHEXs are widely used in industries like food processing, chemicals, and power plants due to their compactness and ease of cleaning [8]. However, they have limitations, such as a maximum pressure of 20.4 bar and an operating temperature of around 150 °C. Lamella-type PHEXs offer higher operational conditions (up to 40.8 bar and 800 °C), but they lack the flexibility of gasketed designs [9].

In recent years, the emergence of nanotechnology has presented new opportunities for improving HEX performance [10,11]. Nanofluids (NFs), consisting of base fluids with suspended nanoparticles (NPs) at the colloidal level, have emerged as a promising approach [12]. They have garnered significant attention due to their unique characteristics and potential to improve heat transfer efficiency [13,14]. By leveraging the properties of the NPs, NFs promise improved TC, HTR, and overall system efficiency [15,16]. NFs demonstrate much greater TC compared to traditional heat transfer fluids. The addition of NPs, such as carbon nanotubes, metallic NPs, or metal oxides, increases the effective TC of the fluid [17,18]. This property allows for more efficient heat transfer, enabling HEXs to achieve higher HTR with the same or reduced surface area [19]. Consequently, the use of NFs can lead to smaller and more compact HEXs, saving space and reducing material costs [20].

A number of studies have investigated the performance of HEXs using different NFs, highlighting the necessity of utilizing NFs in HEXs. Barzegarian et al. [21] studied the application of Al_2O_3/water NF in enhancing the thermal performance (THP) of horizontally oriented shell and tube HEXs under forced circulation. Their results demonstrated a significant improvement in the THP coefficient, with a 21.5 % enhancement at a NF concentration of 0.3 %. Zheng et al. [22] investigated the impact of different NFs containing CuO, Fe_3O_4, SiC, and Al_2O_3 additives on the performance of a corrugated HEX. The findings revealed that NFs significantly enhance heat transfer compared to the base fluid. Among the tested NFs, the water-Fe_3O_4 NF demonstrates the best THP. Compared to water, the CHTC increases by 21.9 %. Conversely, the CuO-water NF exhibits the poorest performance. Additionally, this study presents empirical formulas to predict the THP of various NFs based on experimental data. These formulas are derived to estimate Nusselt number (Nu), which characterizes CHTC and serves as a new approach to predicting the THP of NFs. Du et al. [23] studied the THP of a geothermal HEX utilizing CuO/water NF. Their findings revealed that the utilization of NF in the geothermal HEX resulted in a notable improvement in the HTR and pumping power consumption, which improved by 39.84 % and 16.75 %, respectively. Fares et al. [24] investigated the influence of graphene NFs on CHTC in a vertical shell and tube HEX. The use of NFs increased the THP of the vertical shell and tube HEX. The maximum improvement in the heat transfer coefficient reached 29 % when utilizing 0.2 wt% NFs. Additionally, the average thermal efficiency of the HEX improved by 13.7 % with the use of NF. Bahiraei and Monavari [25] investigated the influence of the shape of the NPs on the performance of the microchannel PHEX using NF. Their results indicated that the NP shape significantly affects HEX performance. The NF containing nanoplate exhibited the highest overall heat transfer coefficient (OHTC), followed by NFs with cylinder, blade, and brick shaped particles, respectively. Jalili et al. [26] conducted a study focusing on the CHTC in a countercurrent double-tube HEX. The researchers conducted experiments using TiO_2 and Al_2O_3 NFs at different concentrations as the cold fluid (CF) in the inner tube, while water served as the HF in the annular space. The study's results indicate that the Al_2O_3 NF exhibited a higher CHTC than TiO_2 and pure water. Increasing the NF concentration from 0.4 % to 6 % led to a 12 % increase in the CHTC. Additionally, HEXs with rectangular and curved fins demonstrated significantly better efficiency (81 % and 85 %, respectively) than those without fins. Hasan [27] evaluated the impact of utilizing a NF containing MWCNTs on the HEX performance. This study showed that, depending on the NF concentration, the OHTC can increase by up to 76.4 % compared to distilled water. The Nu exhibited a maximum increase of 55.6 % at 2 vol%. Additionally, the heat transfer efficiency improved by 19.4 %–38.7 % when using NFs at concentrations up to 2 %. The study by Alklaibi et al. [28] focused on the utilization of a hybrid NF as a coolant in a PHEX. Their findings demonstrated the enhanced heat transfer performance of the hybrid NF in the PHEX. The NF exhibited improved exergy efficiency, THP, effectiveness, and number of transfer units compared to deionized water, indicating its potential for enhancing heat transfer and reducing the size of PHEXs. Ajeeb et al. [29] investigated the enhancement of the PHEX efficiency by using Al_2O_3 NP. Their findings showed that increasing the concentration of NPs led to improved heat transfer, achieving a maximum enhancement of 27 % at 0.2 vol% for distilled water-based Al_2O_3 nanofluid, which was associated with an 8 % rise in ΔP.

A review of the existing literature indicates that the application of NFs in HEXs holds great potential, despite challenges related to the NP stability, cost-effectiveness, and long-term reliability. Overcoming these challenges necessitates thorough examination and resolution. graphene and TiO_2 NPs are commonly employed in the formulation of NFs due to their favorable thermal properties. Using graphene-COOH NFs in PHEXs is a novel approach to enhancing their THP. The exceptional properties of carboxyl graphene NPs, including improved heat transfer efficiency, enhanced fluid flow dynamics, anti-fouling characteristics, and corrosion resistance, offer significant benefits. As research progresses and challenges are addressed, carboxyl graphene NFs have the potential to revolutionize PHEX design and operation. This, in turn, can result in thermal management systems that are not only more efficient but also sustainable across a wide range of industries. To our knowledge, no existing study has directly compared the performance of graphene-COOH nanoplates and TiO_2 NPs in a PHEX. Additionally, no previous studies have been conducted on a pilot scale with minimal error, aiming to simulate real industry conditions. Therefore, the results obtained from this comprehensive evaluation can be replicated to assess the feasibility of industrial implementation.

This study introduces several innovative aspects that enhance thermal engineering and energy efficiency by exploring the use of graphene-COOH and TiO_2 NPs in NFs. It emphasizes the functionalization of graphene with carboxyl groups to improve dispersion stability, addressing a common challenge in NF applications. Additionally, TiO_2, known for its TC and photocatalytic properties, adds further novelty by potentially influencing the behavior of these NPs under varying thermal conditions in PHEXs. The focus on PHEXs as the application for these advanced NFs is significant, as they are widely utilized in industries such as heating, ventilation, and air conditioning, chemical processing, and energy generation due to their compact design and high heat transfer efficiency. The study aims to enhance their performance, which could lead to more efficient heat exchange and reduced energy consumption. Furthermore, the experimental analysis of graphene-COOH and TiO_2 NFs is novel, as it may demonstrate superior performance in enhancing heat transfer in PHEXs compared to traditional methods. The enhancement of heat transfer performance in PHEXs is directly linked to energy efficiency, particularly in renewable energy systems, where improving heat transfer efficiency can lead to lower energy consumption and higher overall system performance. Lastly, the emphasis on NFs aligns with broader sustainability goals, as efficient PHEXs can significantly reduce energy demand, supporting the transition to more sustainable energy solutions.

This study aimed to examine how graphene-COOH nanoplates and TiO_2 NPs affect the THP of a PHEX. NFs were synthesized by incorporating carboxyl graphene and TiO_2 NPs into water at concentrations of 0.01 wt%, 0.03 wt%, and 0.05 wt%. The properties of the NFs, including TC, SHC, density, and viscosity were investigated experimentally at 25 C and 50 C. Subsequently, CHTC, OHTC, *Nu*, ΔP, HEX efficiency, and performance index were determined using available sensors and the collected data.

2. Materials and methods

This section presents comprehensive information on the PHEX system, equations, experimental methods, NF synthesis, and NP characteristics.

Table 1
Characteristics of functionalized graphene and titanium dioxide.

Specification	Value	
Name/Trademark	Carboxyl Graphene	Titanium Oxide
Manufacturer	Platonic Nanotech	Merck
Color	Black	White
Chemical formula	C	TiO_2, anatase
Purity (%)	>98 %	>99 %
Outer diameter (nm)	1–5	10–25
Density (g/cm^3)	2.26	3.9
Specific surface (m^2/g)	190	220–240

2.1. Materials

The NPs used in this experiment are functionalized graphene and titanium dioxide. Functionalized graphene was purchased from Platonic Nanotech. Titanium dioxide was purchased from Merck. Arabic gum, also supplied by Merck, was used as the surfactant. Distilled water served as the base fluid. The characteristics of the functionalized graphene and titanium dioxide NPs are shown in Table 1.

2.2. Experimental setup

The experimental setup includes both open and closed loops. In the open loop, city water flows into the PHEX as the cold flow, while in the closed loop, the NF flows into the PHEX as the hot flow. Fig. 1(a) illustrates a schematic of the setup. The NF is pumped to the PHEX using a circulation pump in the closed loop, and after cooling, it is returned to the NF tank. The collection tank, with a capacity of 5 L, serves as the receiver for return flows from the converter and side flow, featuring two inputs and outputs. Inside the tank, a 3000 W heating element operates at a constant flux for all flow rates. A circulating pump with a performance characteristic of 0.27 kW, a maximum head of 5 m, and a flow rate of 10 L/min is used to pump the NF into the PHEX. The experiment utilizes a gasketed PHEX of the Alfa Laval type with V-shaped grooves. The plates are constructed from 316L stainless steel. The PHEX consists of 21 plates, creating 20 channels for fluid paths. Among these channels, 10 are designated for the HF, while the remaining channels accommodate the CF. Table 2 provides the characteristics of the PHEX, and Fig. 1 (b) displays a picture of the PHEX. To measure the temperatures at the entrance and exit of the PHEX, four Pt-100 thermocouples with a precision of $\pm 0.1\ ^\circ C$ were employed. Additionally, the PHEX was insulated with glass wool to minimize heat leakage. To regulate and monitor the flow rate, four ball-type pressure valves and three quarter-turn type valves were utilized. Experiments were repeated twice at flow rates of 2, 2.4, 2.8, and 3.2 L/min to produce the most consistent results. In all Experiments, the CF flow rate was set at 4 L/min.

2.3. Synthesis of the nanofluid

The synthesis of NF involved a two-step approach. Initially, 500 ml of distilled water was placed in a beaker, and to ensure stability and prevent NP accumulation and precipitation, gum arabic was used at a ratio of 2:1 with respect to the NPs. The mixture was stirred using a stirrer set at 1300 rpm for 30 min. Following this, NPs were added to the base fluid at concentrations of 0.01 wt%, 0.03 wt%, and 0.05 wt%, and the mixture was subjected to rotational stirring using a mixer at 1600 rpm for a period of 2 h. Lastly, to further enhance stability, the synthesized NFs were exposed to ultrasonic waves for 20 min using an ultrasonic probe device (Misonix Sonicator XL2020, USA). This process established

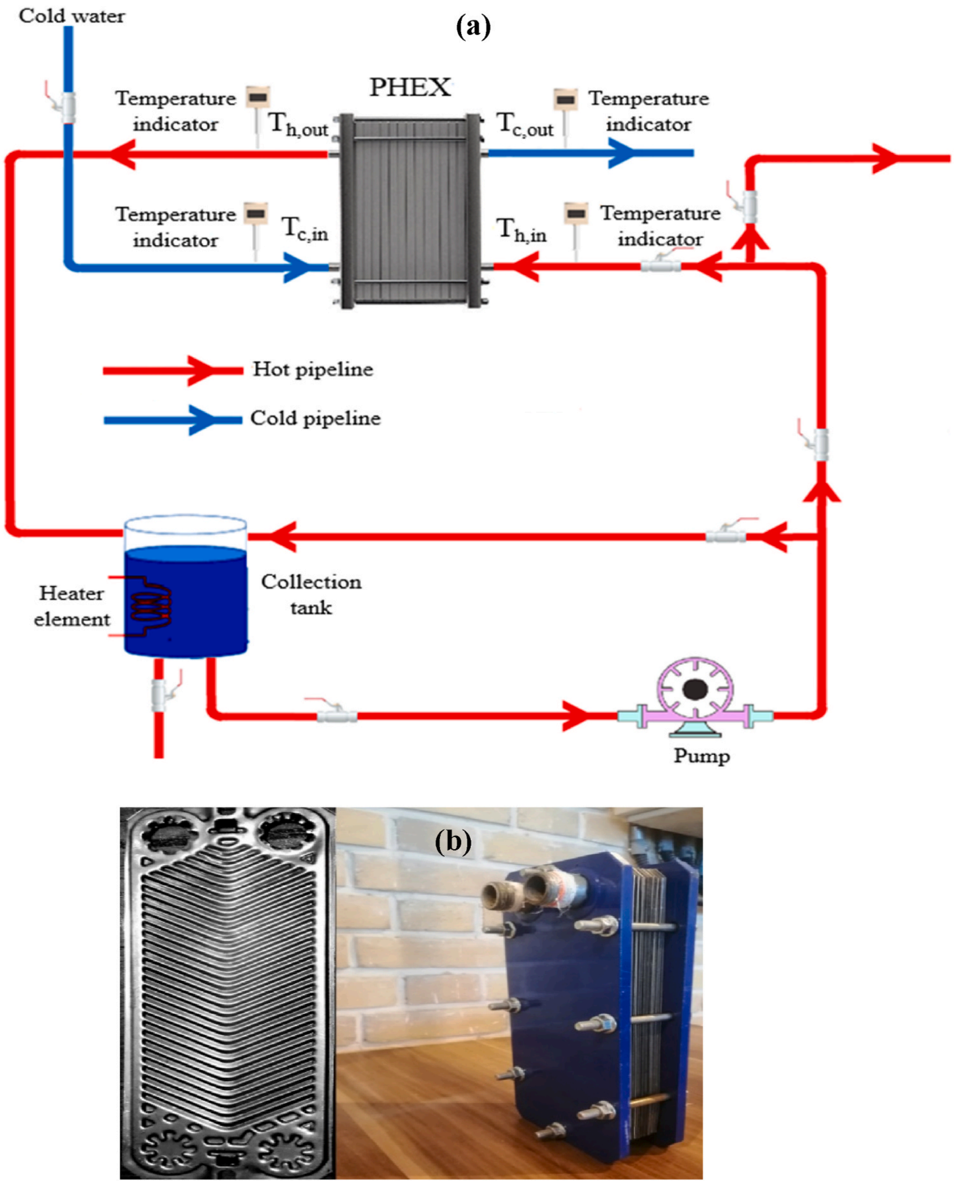

Fig. 1. (a) Schematic diagram of the experimental setup and (b) picture of PHEX.

Table 2
The characteristics of PHEX.

Parameter	Amount
Width of plates (w)	72 mm
Length of plates (L)	155 mm
Number of plates (N)	21
Depth of plates (b)	1.5 mm
Thickness of plates (t)	0.5 mm
Diameter of ducts (D_p)	19.2 mm
Angle along of plates (β)	60°
Diameter of ducts (D_p)	19.2 mm
Corrugation pitch (P_c)	5.5 mm
Surface enlargement ratio	1.044

essential relationships to determine the precise amount of the NPs needed and attain the desired concentration. To ascertain the exact quantity of the NPs required and achieve the desired concentration, equations (1) and (2) were utilized.

$$\varphi\ (\text{wt.\%}) = \frac{m_p}{m_p + m_{bf}} \times 100 \tag{1}$$

$$\varphi = \phi . \frac{\rho_p}{\rho_{nf}} \tag{2}$$

These equations involve variables denoted as φ, ϕ, ρ_p, ρ_{bf}, and ρ_{nf} which represent the NPs mass fraction, NPs volume fraction, NPs density, water density, and NF density, respectively. The subscripts bf, nf and p are water, NF and NPs, respectively. Additionally, m_p and m_{bf} represent the mass of the NPs and water, respectively. NFs containing TiO_2 NPs with concentrations of 0.01 wt%, 0.03 wt%, and 0.05 wt% were respectively labeled as T1, T2, and T3. Similarly, NFs containing graphene-COOH nanoplates with concentrations of 0.01 wt%, 0.03 wt%, and 0.05 wt% were respectively labeled as G1, G2, and G3.

2.4. Characterization

In this research, various analytical methods were utilized to characterize NPs. Fourier transform infrared spectroscopy (FTIR; Bruker/TENSOR 27, Germany) was used to assess the chemical composition and identify the functional groups on the surfaces of the NPs. Scanning electron microscopy (SEM; TESCAN/MIRA3, Czech Republic) offered in-depth insights into the morphology, size, and shape of the NPs, enabling a detailed analysis of their surface characteristics. Energy dispersive X-ray (EDX; TESCAN/MIRA3, Czech Republic) analysis was used to identify the elemental makeup of the materials. Furthermore, X-ray diffraction (XRD; Bruker AXS/D8 ADVANCE, Germany) was employed to investigate the crystalline structure and phase composition of the NPs, providing important information regarding their crystallinity and atomic arrangement. The thermal characteristics, including TC and SHC of the NFs with an accuracy of ±5 %, were analyzed using the KD2 pro thermal property analyzer produced by Decagon. Density (ρ) was analyzed using a density meter (KEM DA-650, accuracy: 2×10^{-5} g cm^{-3}, and temperature rang 0–96 °C). The kinematic viscosities of the NFs were measured using a Cannon-Fenske Opaque viscometer.The kinematic viscosity of the NFs at different temperatures was evaluated using a precision temperature-controlled bath that ensured a stable temperature. Each test for TC, SHC, density, and viscosity was conducted three times to ensure the accuracy of the results. Zeta potential (Nanotrac Wave model, Microtrc, USA) analysis provides valuable information about the stability and behavior of these particles in solution.

2.5. Data reduction

A series of calculations is needed to determine the HTR in the HEX and analyze the performance of NFs. The CHTC, OHTC, *Nu*, efficiency, and ΔP play crucial roles in evaluating the effectiveness of a HEX utilizing NF. In this section, relations for calculating these parameters are introduced. Prior to investigating the heat transfer properties of the NF, it is necessary to evaluate the physical properties of both the NF and water.

Based on the mass flow rate, SHC, and temperature difference between the CF and NF, the sensible heat lost by the HF and the sensible heat gained by the CF were estimated using the following equations [30]:

$$Q_h = \dot{m}_h . C_{p,h} . (T_{h.i} - T_{h.o}) \tag{3}$$

$$Q_c = \dot{m}_c . C_{p,c} . (T_{c.o} - T_{c.i}) \tag{4}$$

$$Q_{ave} = \frac{Q_c + Q_h}{2} \tag{5}$$

where 'c' and 'h' indicate the cold and hot flows, respectively. Q (W) represents the amount of absorbed or dissipated heat. $T_{h.i}$, $T_{h.o}$, $T_{c.i}$, and $T_{c.o}$ are the inlet HF temperature, the outlet HF temperature, the inlet CF temperature and the outlet CF temperatures, respectively. $\dot{m}_h$ and $\dot{m}_c$ represent the mass flow rate of hot and CF, respectively.

The OHTC was calculated as follows [31]:

$$Q_{ave} = U.F.A.\Delta T_{LMTD}, U = \frac{Q_{ave}}{F.A.\Delta T_{LMTD}} \tag{6}$$

where U is the OHTC (W/m^2K), *A* is the heat transfer surface (m^2), *F* is the temperature correction factor that is considered equal to 1 in the case of counterflow in the HEX. ΔT_{LMTD} represents the average logarithmic temperature which is defined as follows [31]:

$$\Delta T_{LMTD} = \frac{(T_{h,i} - T_{c,o}) - (T_{h,o} - T_{c,i})}{\ln\left(\frac{T_{h,i} - T_{c,o}}{T_{h,o} - T_{c,i}}\right)} \tag{7}$$

To calculate the overall area of heat transfer, a series of relations specific to the grooved plate exchanger is needed. For this reason, a correction factor called the surface increase ratio (χ) was defined as follows [32]:

$$\chi = \frac{1}{6}\left\{1 + \left(1 + \left(\frac{\pi}{2\cos(\alpha)}\right)^2 \gamma^2\right)^{0.5} + 4\left(1 + \left(\frac{\pi}{2\sqrt{2}\cos(\alpha)}\right)^{0.5} \gamma^2\right)^{0.5}\right\} \tag{8}$$

where γ represents the aspect ratio of the PHEX channels and is defined as follows:

$$\gamma = \frac{2b.\cos(\beta)}{P_c} \tag{9}$$

The area (A) was obtained using the following equation.

$$A = (N-2).\chi.w.L \tag{10}$$

where N, w, L, and χ represent the number of plates, width, length, and surface increase ratio respectively, as presented in Table 2.

Eq. (11) was used to calculate the hydraulic diameter:

$$d_{hy} = \frac{2b}{\chi} \tag{11}$$

The superficial velocity of cold and hot flow inside the channels was calculated using Eq. (12) and Eq. (13), respectively [33].

$$G_c = \frac{\dot{V}_c}{N_c wb} \tag{12}$$

$$G_h = \frac{\dot{V}_h}{N_h wb} \tag{13}$$

In these equations G_c refers to the superficial velocity (the velocity at which the two-phase fluid appears to be moving) of the cold flow, and G_h represents the superficial velocity of the hot flow. N_c and N_h denote the number of plates associated with the cold and hot flows, respectively. w refers to the width of the plate, and *b* represents the depth of the plate. Additionally, the mass flow rates of the cold and HF are indicated as $\dot{V}_c$ and $\dot{V}_h$, respectively.

Eq. (14) and Eq. (15) were used to obtain Reynolds (Re) numbers of cold and hot flow, respectively [33].

$$Re_c = \frac{\rho_c G_c d_{hy}}{\mu_c} \tag{14}$$

$$Re_h = \frac{\rho_h G_h d_{hy}}{\mu_h} \tag{15}$$

Eq. (16) was used to calculate the Prandtl number (Pr).

$$Pr = \frac{\mu C_p}{k} \tag{16}$$

The experimental equations, which represent the *Nu* for the studied PHEX, are presented in the following equation:

$$Nu_d = a.Re_d^b.Pr^{0.33} \tag{17}$$

Eq. (18) was used to obtain Peclet number (*Pe*).

$$Pe = RePr \tag{18}$$

The heat transfer coefficient (h) was obtained with the following equation.

$$h = \frac{Nuk}{d_{hy}} \tag{19}$$

where k is the TC of the fluid flow.

CHTC of the HF is calculated from Eq. (20) [34].

$$\frac{1}{h_h} = \frac{1}{U} - \frac{1}{h_c} - \frac{t}{k} \tag{20}$$

where t is the thickness of the plate and k is the TC of the plate.

The ΔP inside the PHEX was calculated using the following equation [33].

$$\Delta P = \left(\frac{2fL_pN_pG^2}{\rho d_{hy}}\right) + 1.4\left(\frac{N_pG_p^2}{2\rho}\right) + \rho g\left(L_p + d_{hy}\right) \tag{21}$$

where N_p and L_p are the number of passes in the plate and the vertical distance between the ducts (length of the plate). G_p is the superficial velocity in the input/output ports and is defined as Eq. (22). f is the friction coefficient and is defined as Eq. (23) [35].

$$G_p = \frac{4\dot{V}}{\pi D_p^2} \tag{22}$$

$$f = \frac{3.24}{Re^{0.457}} \tag{23}$$

The HEX efficiency was calculated using the following equation [33].

$$\varepsilon = \frac{T_{h,i} - T_{h,o}}{T_{h,i} - T_{c,i}} \tag{24}$$

3. Results

In this section, the characterization of the NPs is discussed, and the thermophysical properties of the NFs are presented. The THP of graphene-COOH/water and TiO_2/water NFs in a PHEX is presented. The parameters examined include the CHTC, Nu, Pe, Pr, OHTC, PHEX efficiency (ε), friction coefficient (f), and ΔP.

3.1. Characterization results

SEM analysis was conducted to examine the structure and morphology of the NPs. Fig. 2(a) and (b) show SEM images of graphene-COOH nanoplates. Fig. 2(c) and (d) display SEM images of TiO_2 NPs. The SEM images of graphene-COOH reveal a complex morphology characterized by thin, crumpled sheets that exhibit a high degree of surface roughness due to the presence of carboxyl functional groups. The image displays irregularly shaped graphene flakes with varying thicknesses, indicating the presence of multiple layers, which is essential for enhancing the material's surface area and reactivity. The high aspect ratio of the graphene sheets, combined with the functionalization, suggests significant potential for applications in fields such as energy storage, sensors, and nanocomposites. SEM images of the TiO_2 NPs show that the particles are mostly spherical in shape with good dispersion, indicating that the synthesis method effectively produces uniform NPs. Furthermore, it is observed that there is less aggregation of the NPs, which is a desirable feature for many applications, as it allows for better accessibility of the particles in different environments. This reduction in aggregation may be attributed to the careful control of the synthesis parameters, including the choice of precursors and reaction conditions.

According to Fig. 3(a), the XRD examination of graphene-COOH indicates a peak in the spectrum at 2θ ≈ 26.5° corresponding to the

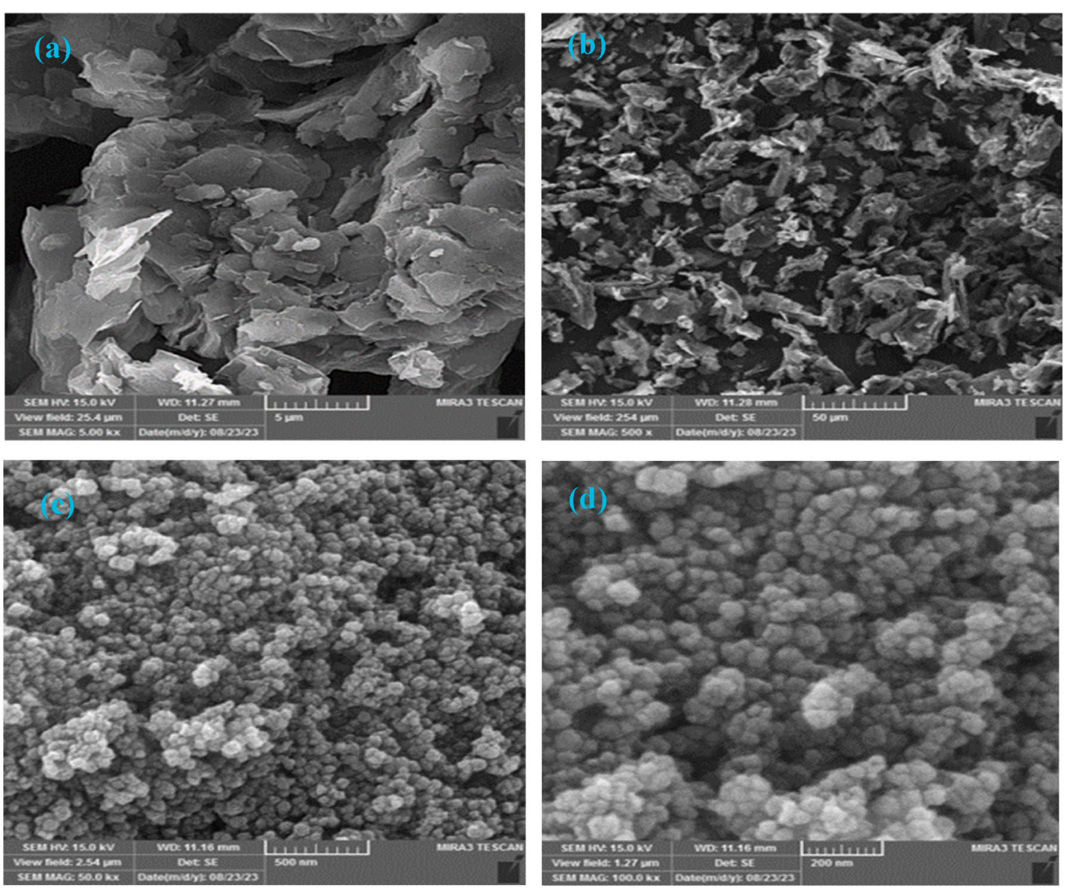

Fig. 2. SEM images of (a), (b): graphene-COOH and (c), (d): TiO_2.

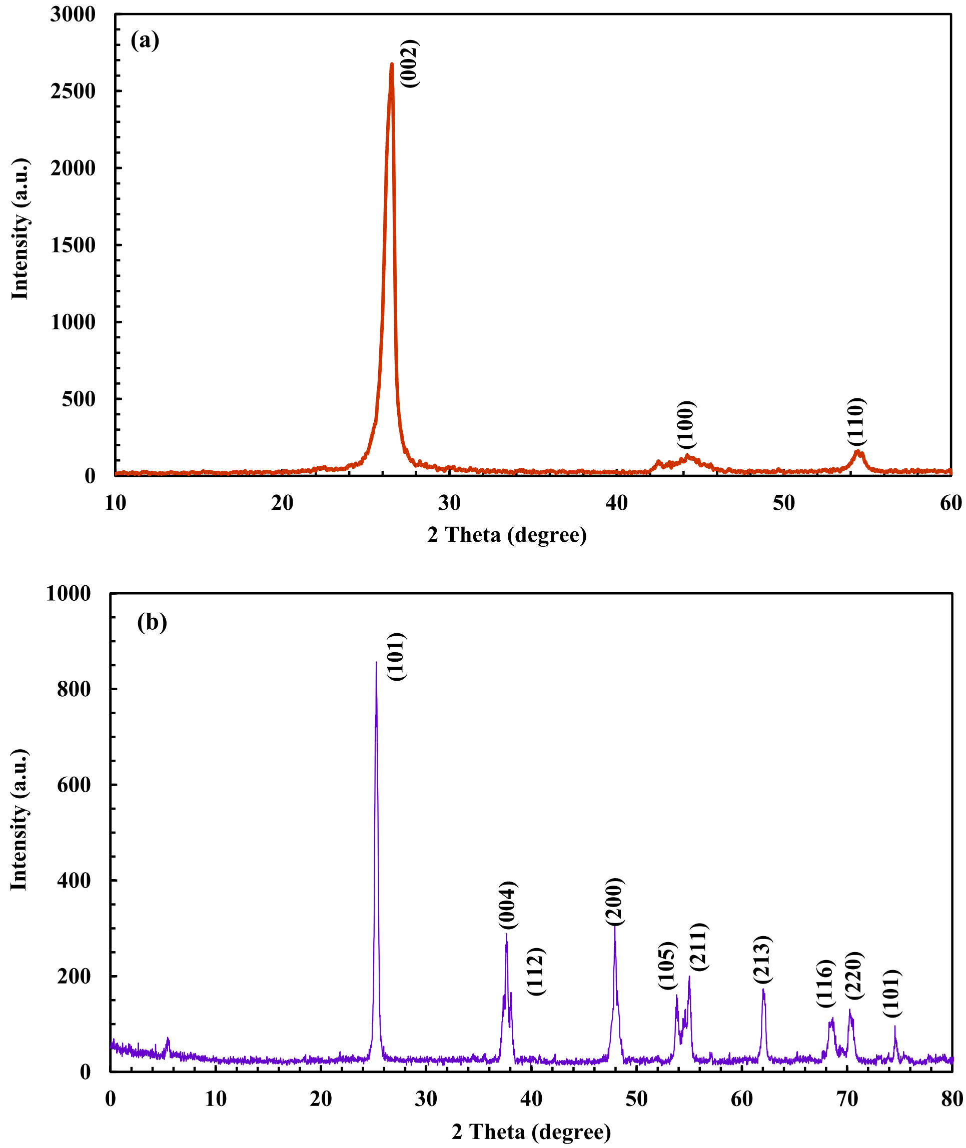

Fig. 3. XRD analysis of (a) graphene-COOH and (b)TiO_2.

(002) planes. Additionally, there are weak peaks at angles of 44.54° and 54.44°, with Miller indices of (100) and (110), respectively. These peaks indicate the crystal structure and provide evidence of the layered nature of graphene sheets. According to Fig. 3(b), the XRD examination reveals the presence of anatase phases in TiO_2, which corresponds to the patterns observed in JCPDS No. 01-071-1167. The anatase phase pattern exhibits prominent peaks at angles of 25.2, 37.7, 38.07, 47.95, 53.78, 54.99, 62.98, 68.39, 70.26, and 74.55°, corresponding to the crystallographic planes (101), (004), (112), (200), (105), (211), (213), (116), (220), and (215), respectively [36,37]. The absence of unexplained peaks confirms the high purity of the produced anatase NPs. Moreover, the broad nature of the diffraction peaks indicates that the NPs have very small crystallite sizes.

Fig. 4(a) and (b) show the FTIR analysis of graphene-COOH and TiO_2 NPs, respectively. The FTIR analysis of graphene-COOH reveals a prominent broad peak at 3433.38 cm^{-1} in the high-frequency region, which corresponds to the stretching of the O-H bond. The peak observed in the spectrum at 3413.57 cm^{-1} suggests the presence of hydroxyl (OH) groups in graphene-COOH. Additionally, the peaks detected at 2923 cm^{-1} and 2856.46 cm^{-1} can be attributed to the asymmetric and symmetric stretching vibrations of CH_2 (methylene) bonds, respectively [38]. The peaks observed at 876.68 cm^{-1}, 711.16 cm^{-1}, and 585.92 cm^{-1} are attributed to C-H vibrations [39]. The peak observed at 1630.58 cm^{-1} in the spectrum is attributed to the stretching and bending vibrations of O-H groups present in water molecules that are adsorbed onto graphene-COOH [40]. The peak at 1066.56 cm^{-1} provides information about the C-O-C stretching of alkoxy groups [40]. The FTIR spectrum for the TiO_2 NPs, as shown in Fig. 4(b), features a peak at 449.06 cm^{-1}, which is associated with Ti-O-Ti stretching vibrations. This peak confirms the existence of titanium oxide bonds within the NPs. Furthermore, peaks at 806.29 cm^{-1} and 1313.02 cm^{-1} relate to Ti-O stretching vibrations, offering significant insights into the bonding structure between titanium and oxygen in the TiO_2 lattice. The peak at 1629.82 cm^{-1} indicates the presence of adsorbed water molecules. Moreover, a prominent peak at 3413.57 cm^{-1} in the spectrum suggests O-H stretching vibrations, pointing to the presence of hydroxyl groups or adsorbed water on the surface of the TiO_2 NPs.

The zeta potential is a commonly utilized measure to assess the degree of electrostatic interaction among colloidal particles. Therefore, it serves as an indicator of the solution's colloidal stability. Fig. 5 illustrates the results of zeta potential analysis performed on NFs with different weight percentages after preparation and after 7 days. As the mass concentration of the NPs in the NF increases, it is typically noted that the absolute value of the zeta potential, expressed in millivolts,

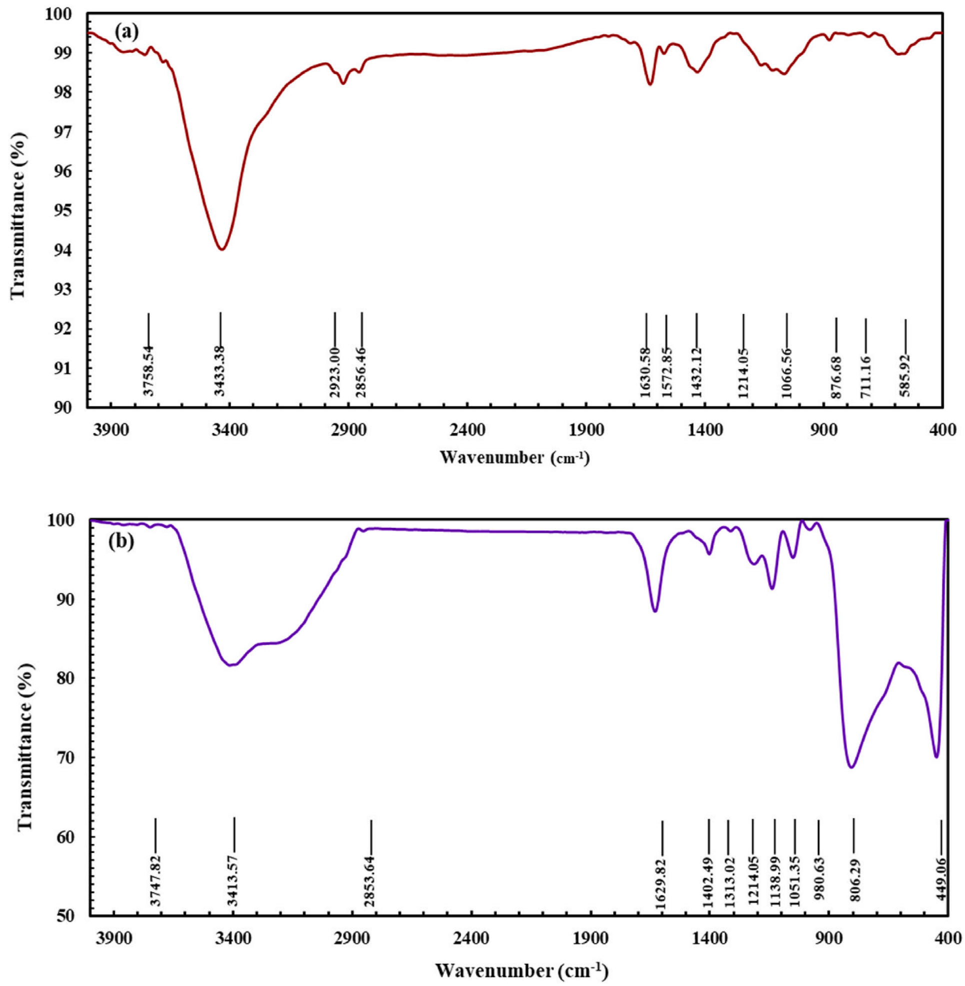

Fig. 4. FTIR analysis of (a) graphene-COOH and (b) TiO_2.

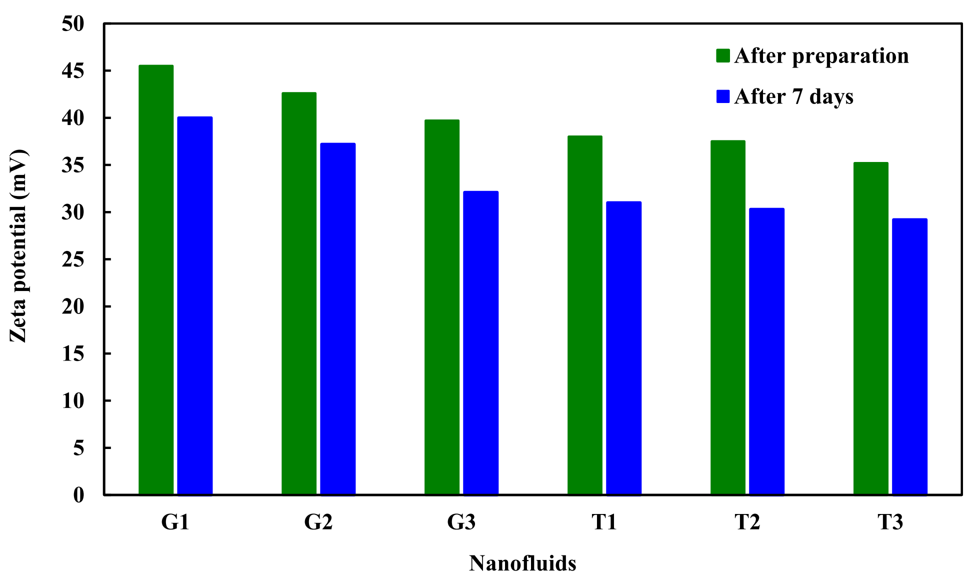

Fig. 5. Zeta potential values for nanofluids in three different mass concentrations after preparation and after 7 days.

tends to decline. This decrease occurs because the higher mass concentration of the NPs results in a greater presence of the NPs, leading to intensified van der Waals interactions among them. As a result, there is a heightened likelihood of agglomeration and settling within the NF, causing reduced stability concerning mass concentrations. Additionally, the stability of both NFs wanes over time due to potential factors such as NPs aggregation, sedimentation, and the gradual reduction in electrostatic repulsion forces. Nevertheless, the drop in zeta potential value after 7 days still does not compromise the overall stability of NF, as the value remains above 30 mV. The zeta potential of the graphene-COOH NF samples surpasses that of the TiO_2 NF samples. For both types of NFs, at all concentrations, the zeta potential exceeds 35.2 mV (immediately after preparation) and 29.2 mV (after 7 days), signifying the excellent stability of the employed NFs.

3.2. Nusselt number correlation

The CHTC for the CF is needed to determine the CHTC for the HF. Eq. (19) can be applied to forecast the CHTC in HEXs. Experimental studies were conducted using water as both the HF and CF to determine the coefficients a and b. In the scenario where the working fluid and plate geometry remain constant, it can be assumed that the constants "a" and "b" in Eq. (17) should be identical for both sides within the same flow regime. This assumption is based on the premise that the flow conditions and characteristics are symmetrical and consistent throughout the system. Initially, Eq. (6) can be utilized to calculate the OHTC. An initial estimate for the CHTC of cold water was obtained using the equation proposed by Kumar [35,41].

$$Nu = 0.306 Re^{0.529} Pr^{0.33} \quad 20 < Re < 400 \tag{25}$$

$$h = \frac{Nu.k}{d_{hy}} \tag{26}$$

The CHTC for hot water and the Nu can be obtained using Eqs. (20) and (19), respectively. By analyzing the relationship between $Nu_h / Pr_h^{0.33}$ and Re_h, constants a and b were determined. Then, the values of a and b in Eq. (25) were replaced instead of 0.306 and 0.529 to obtain a new value of the CHTC of CF. After finding the CHTC of the new CF, the CHTC and *Nu* of the new HF can be calculated using Eqs. (20) and (19). Through the analysis of the relationship between the $Nu_h / Pr_h^{0.33}$ and Re_h new values for the parameters "a" and "b" were derived. After 36 iterations, the new values of "a" and "b" showed minimal deviation from the initial values, indicating convergence. These new values were then accepted as the final results. Consequently, the relationship used to calculate the Nu for cold water can be expressed as follows:

$$Nu = 0.0494 Re^{0.878} Pr^{0.33} \tag{27}$$

To validate the accuracy of this correlation, the Nu of the HF was calculated twice. First, it was calculated using Eq. (19) (Nu_{ca}), and then using Eq. (27) (Nu_{th}). The results obtained from these calculations are depicted in Table 3. As shown in Table 3, when comparing the values obtained from the two different methods, there is no significant disparity. The most notable difference observed in the values was 12.73 %, when the Pe was 517.03. According to Table 3, as Re_h increased to 217.07, the difference between Nu_{th} and Nu_{ca} was reduced to 0.68 %. Therefore, Eq. (27) provides acceptable results for Re_h values ranging from 137 to 217 when Re_c is 200 in this HEX. This approach is based on the research conducted by Huang et al. [42]. Researchers have proposed numerous correlations to predict the heat transfer performance in PHEXs when water is used as the working fluid. Fig. 6 presents a comparison between the newly proposed Eq. (27) and four other empirical correlations, including those by Kumar et al. [41], Huang et al. [42], Pantzail et al. [43], and Durmuş et al. [44]. Table 4 summarizes the referenced correlations. According to Table 3, Eq. (27) offers the most accurate prediction for laminar flow, with all calculated data closely matching the experimental data. Fig. 6 indicates that Kumar et al.'s equation [41] provides accurate predictions, with an error range of approximately ±13 %. On the other hand, the correlations proposed by Huang et al. [42], Pantzail et al. [43], and Durmuş [44] deviate significantly from the experimental data, consistently underestimating the results. The deviations observed between this study and previous correlations and experiments can be attributed to variations in experimental settings such as geometric parameters and PHEX fabrication processes, temperature range, flow rate, and Reynolds numbers, which can significantly affect the performance of the working fluids.

Table 3
Comparison of the *Nu* of the fluid based on Eqs. (27) and (19) in $Re_c = 200$.

Re_h	Pr_h	Pe_h	Nu_{th}	h_{th}	Nu_{ca}	h_{ca}	Error (%)
137.1	3.77	517.03	5.76	1280.57	5.02	1117.6	12.73
158.4	3.93	623.72	6.63	1468.36	6.03	1335.43	9.05
170.2	4.32	736.10	7.28	1597.7	7.11	1560.52	2.33
193.3	4.35	842.03	8.16	1789.33	7.64	1674.79	6.40
217.07	4.36	947.52	9.04	1981.99	8.21	1799.59	9.20

3.3. Thermal performance

Table 5 provides the average thermophysical property values of water and NFs at 25 °C and 50 °C. The addition of graphene-COOH nanoparticles resulted in an impressive increase in thermal conductivity by 29.6 %. This significant enhancement can be attributed to the superior thermal properties of graphene, which enhances heat transfer capabilities in fluid applications. In contrast, the addition of TiO_2 led to a smaller increase in thermal conductivity of only 11.2 %. This disparity indicates that graphene-COOH is considerably more effective in improving the thermal conductivity of the base fluid compared to TiO_2, suggesting that graphene-COOH may be a more suitable option for applications where thermal efficiency is critical. While graphene-COOH improved thermal conductivity, it also resulted in a modest increase in viscosity of 2.14 %. In comparison, the addition of TiO_2 caused a more pronounced increase in viscosity, reported at 3.15 %. This indicates that although both nanoparticle additions raised the fluid viscosity, TiO_2 had a greater effect. The increased viscosity associated with TiO_2 could be a consideration for applications where low flow resistance is desired, as it may necessitate higher pumping energy. The density of the base fluid also increased with the addition of nanoparticles. The density rose by 2.57 % for graphene-COOH and by 4.18 % for TiO_2. This suggests that TiO_2 has a more significant effect on density enhancement than graphene-COOH, which could impact the overall fluid dynamics and pressure drop in heat transfer systems. The increased density signifies an alteration in the physical properties of the base fluid, which may require adjustments in system design or operational parameters. Adding a small amount of graphene-COOH (0.05 wt%) to the base fluid significantly enhances its thermal conductivity and slightly increases its viscosity and density. These changes indicate that graphene-COOH effectively improves the fluid's performance in heat transfer applications, with minimal adverse effects on flow and handling characteristics. In contrast to the increases observed in TC, viscosity, and density, the SHC decreased with both additives. The addition of 0.05 wt% of graphene-COOH resulted in a 3.46 % decrease, while the addition of TiO_2 led to a 4.02 % reduction in SHC. This reduction indicates that both types of nanoparticles diminish the ability of the fluid to store thermal energy, which is a critical property in thermal management systems. The decrease in SHC must be considered when evaluating the overall thermal performance of the fluid in applications. With the rise in temperature, the viscosity of the NF containing graphene-COOH decreased. From 25 °C to 50 °C, viscosity decreased by 35.9 % for base fluid and by 35.73 %, 35.55 %, and 35.08 % for 0.01, 0.03, and 0.05 wt%, respectively. These results align well with those reported in the literature [45, 46]. The viscosity of the base fluids played a crucial role in the TC of NFs; enhancements in TC were greater when the base fluid had lower viscosity [47]. An increase in viscosity could lead to a rise in ΔP and pumping power requirements, particularly in industrial applications. For NFs containing 0.01, 0.03, and 0.05 wt% of TiO_2 NPs, viscosity decreased by 35.15 %, 35.13 %, and 35.26 %, respectively, with the increase in temperature from 25 °C to 50 °C.

The variations in heat transfer rates as a function of superficial velocity for both the hot and cold sides of PHEX are illustrated in Fig. 7(a) and (b). With increasing superficial velocity the heat transfer reate

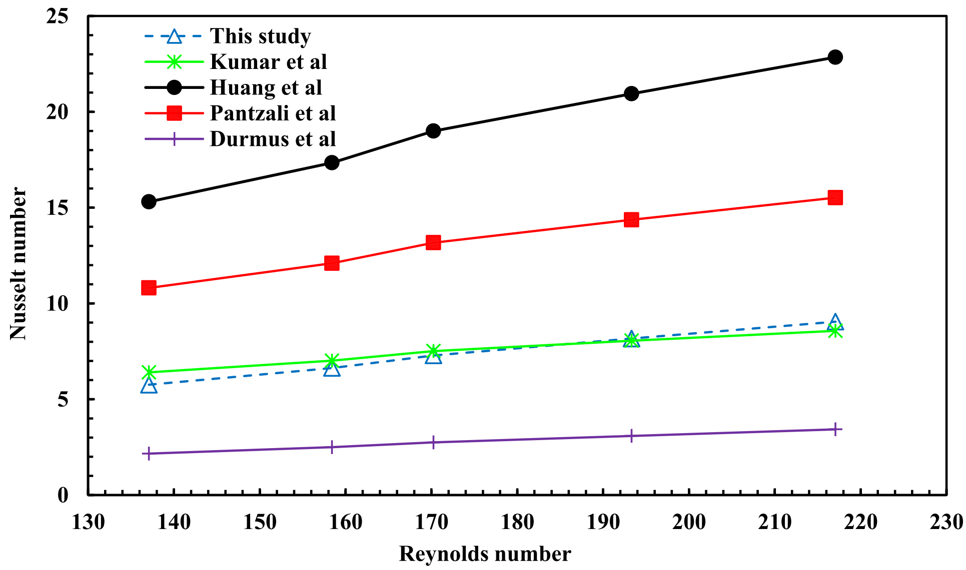

Fig. 6. Comparison of Eq. (27) with four existing correlations: Kumar et al. [41], Huang et al. [42], Pantzail et al. [43], and Durmuş et al. [44].

Table 4
Some *Nu* correlations used in PHEXs.

Ref	Correlations	Comments
Present study	$Nu = 0.0494Re^{0.878}Pr^{0.33}$	$120<Re_h<300$, $Re_c = 200$, $\beta = 60^{\circ}$, $A = 0.22m^2$, surface enlargement ratio = 1.04, $P_c = 5.5$ mm, $d_h = 2.87$ mm
Kumar et al. [41]	$Nu = 0.306Re^{0.529}Pr^{0.33}$	$20<Re<400$, surface enlargement ratio = 1.17, $\beta = 60^{\circ}$
Huang et al. [42]	$Nu = 0.2302Re^{0.745}Pr^{0.4}$	$20<Re_h<400$, surface enlargement ratio = 1.237, $\beta = 60^{\circ}$, $A = 0.234m^2$, Plate thickness = 0.0003m, L = 0.15m, w = 0.07m
Pantzali et al. [43]	$Nu = 0.247Re^{0.66}Pr^{0.4}$	$20<Re_c<400$, $240<Re_h<335$, plate length = 0.2m, plate width = 0.075m, thickness = 0.0005m, $A = 0.26m^2$, $\beta = 60^{\circ}$
Durmus et al. [44]	$Nu = 0.0169Re^{0.897}Pr^{0.33}$	$10<Re<1000$, $2.2<Pr<6.8$

deceased for water and nanafluids. However, the addition of nano-additives led to enhance heat transfer rate in both hot and cold side of PHEX. This observed trend emphasizes the influence of superficial velocity on the thermal performance of the heat exchanger. As superficial velocity increases, the flow dynamics within the heat exchanger tend to become more turbulent, which may initially result in a reduction in heat transfer efficiency for conventional fluids such as water. This reduction could be attributed to the development of secondary flows that interfere with direct heat transfer. In contrast, the incorporation of nanofluids, which contain nanoparticles that enhance thermal properties, counteracts this decline. The nanoparticles improve thermal conductivity and convective heat transfer coefficients, thereby increasing the overall heat transfer performance in PHEX, even at higher superficial velocities when compared to water.

Fig. 8 illustrates the variations in the Nu concerning the Pe for NFs and water. It is evident from Fig. 8 that the Nu increases with the Pe for each NP concentration. This is because the Nu number influences the Pe, as both are related to the Re and Pr. The Re, in turn, depends on the fluid velocity within the PHEX. Consequently, the increase in the Nu can be explained by the increase in the Pe. For example, the Nu increased from 7.62 for pure water to 8.92 for the T3 sample, and further to 8.98 for the G3 sample. This can be attributed to the presence of the NPs, which facilitate better and more uniform heat distribution through their random movement within the base fluid. As the concentration of the NPs increases, their interaction and impact also increase. Additionally, the relative movement and penetration of the NPs within the channels of the HEX can lead to faster heat transfer to the wall. This phenomenon is more pronounced at higher Peclet numbers, resulting in a steeper slope on the Nu graph. This is due to the intensified random movements of the NPs in the more turbulent flow of the NF within the HEX than the base fluid. The increased random movements and dispersion effects at high flow rates enhance the mixing-induced disturbances, producing a temperature profile closely resembling the flow profile. Conversely, at lower flow rates, the likelihood of NP accumulation within the NF rises. Thus, at lower Peclet numbers, the increase in the Nu is comparatively smaller. The highest increase in the Nu value was observed for the graphene-COOH/water NF at 0.05 wt%, showing a 21.35 % increase compared to water. By increasing the concentration of graphene-COOH to 0.01 wt %, 0.03 wt%, and 0.05 wt% in water, the *Nu* increased by 13.21 % (at Pe = 832.3), 16.75 % (at Pe = 825.8), and 17.47 % (at Pe = 810.8), respectively. By increasing the concentration of TiO_2 to 0.01 wt%, 0.03 wt%, and 0.05 wt% in water, the *Nu* increased by 2 % (at Pe = 728.9), 7.9 % (at Pe = 731.1), and 12.7 % (at Pe = 729.26), respectively.

Table 5
Values of TC, SHC, dynamic viscosity, and density for nanofluids at 25 °C and 50 °C.

Sample	25 °C				50 °C			
	k (W/m.K)	C_p (kJ/kg.C)	μ 10^{-3}(Pa.s)	ρ (g/cm^3)	k (W/m.K)	C_p (kJ/k.C)	μ 10^{-3}(Pa.s)	ρ (g/cm^3)
Water	0.607	4.180	0.855	0.9973	0.640	4.192	0.548	0.9905
T1	0.634	4.117	0.862	1.007	0.652	4.129	0.559	1.000
T2	0.652	4.075	0.871	1.021	0.671	4.087	0.565	1.014
T3	0.675	4.012	0.882	1.039	0.698	4.027	0.571	1.032
G1	0.693	4.142	0.859	1.002	0.722	4.154	0.552	0.9952
G2	0.723	4.092	0.869	1.013	0.765	4.104	0.560	1.006
G3	0.787	4.035	0.875	1.023	0.842	4.046	0.568	1.016

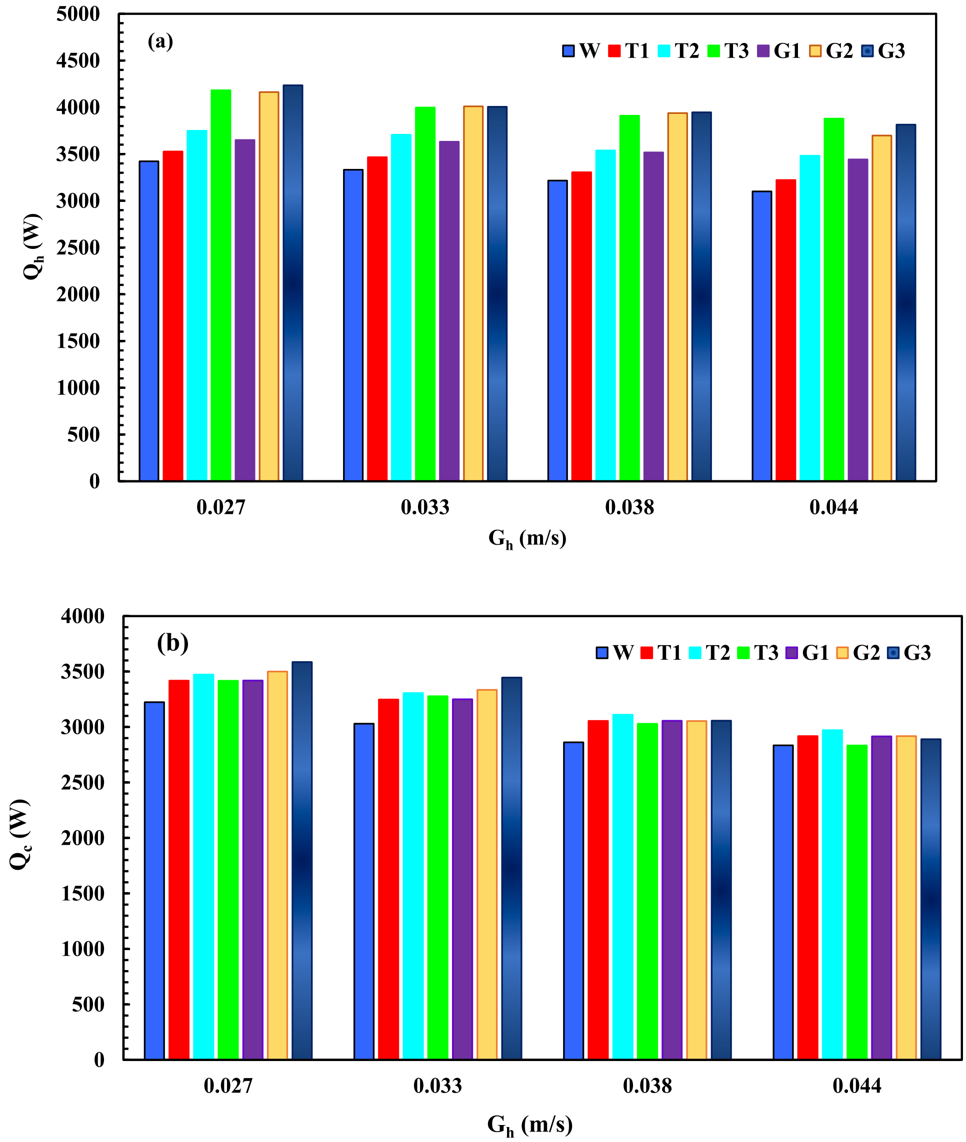

Fig. 7. The variations of heat transfer rate with the superficial velocity of the hot flow (a): Q_h, hot side; (b): Q_c, cold side.

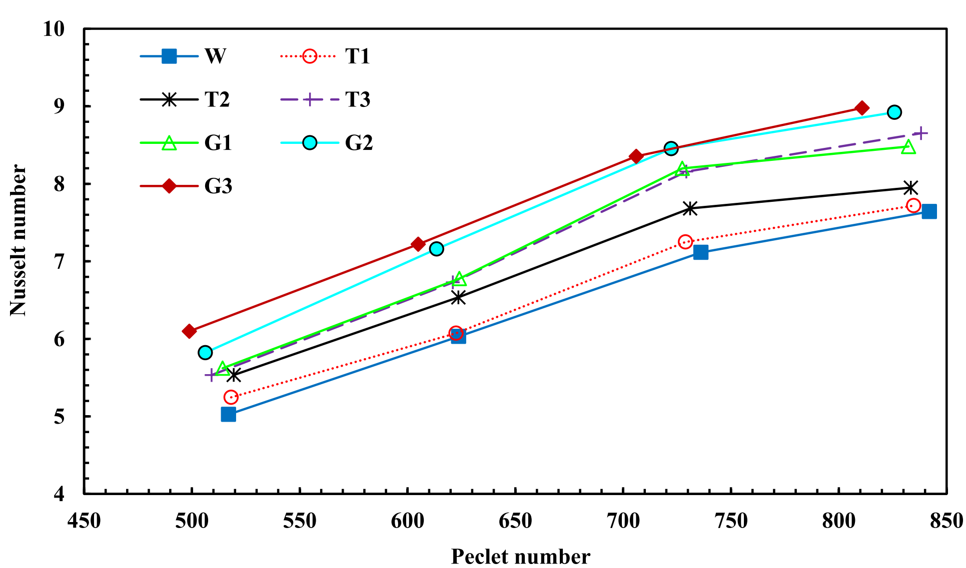

Fig. 8. Variations in the Nu with the Pe for graphene-COOH/water and TiO_2/water nanofluids at different concentrations compared to water.

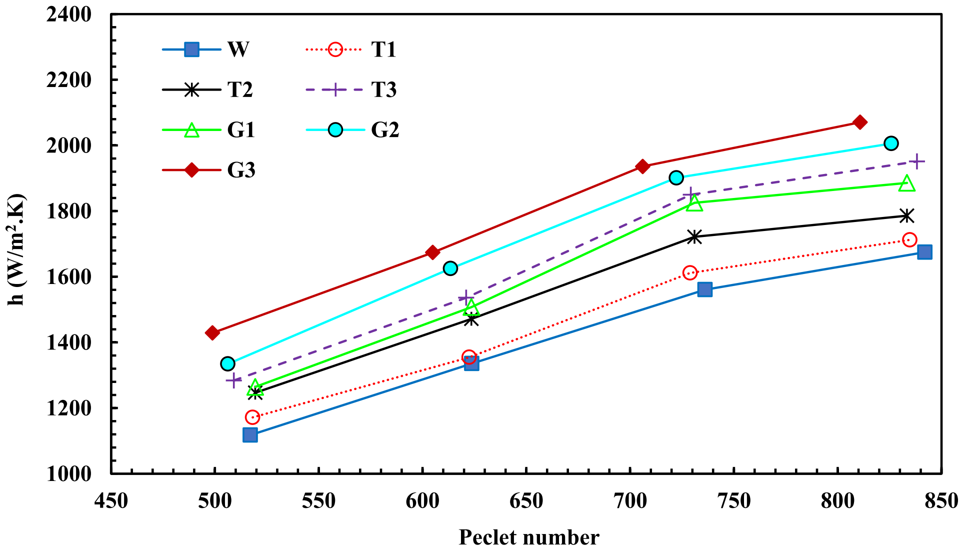

Fig. 9. Variations in the CHTC with the Pe for graphene-COOH/water and TiO_2/water nanofluids at different concentrations compared to water.

According to Fig. 8, among the NPs, graphene-COOH had the most significant impact on the *Nu* compared to TiO_2 NPs.

The CHTC in terms of flow rate is displayed in Fig. 9. The addition of graphene-COOH and TiO_2 NPs to water led to an increase in the CHTC. With the addition of 0.01 wt%, 0.03 wt%, and 0.05 wt% of graphene-COOH in water, the CHTC increased by 16.50 % (at Pe = 832.3), 19.76 % (at Pe = 825.8), and 23.62 % (at Pe = 810.8), respectively. By increasing the concentration of TiO_2 to 0.01 wt%, 0.03 wt%, and 0.05 wt % in water, the CHTC enhanced by 2.24 % (at Pe = 834.7), 6.63 % (at Pe = 833.4), and 14.16 % (at Pe = 838.2), respectively. The reason for this can be attributed to two factors. Firstly, the dispersion of the NPs in the base fluid enhances the heat transfer quality due to their random movement within the fluid. Secondly, the addition of the NPs increases the TC of the fluid. According to Eq. (26), the CHTC has a direct relationship with the CHTC of the fluid, increasing the heat transfer coefficient [48]. This increase is due to the formation of a layer around the NP, referred to as a nanolayer, which exhibits TC similar to that of the NP, consequently boosting the TC of the NF [49]. Additionally, long clusters of the NPs are formed within the NF, facilitating faster heat transfer along these pathways and further enhancing the TC of the NF [50]. Between graphene-COOH and TiO_2, graphene-COOH has high TC. The highest value was attributed to the concentration of 0.05 wt% graphene-COOH equal to 2070.42 W/m^2K. Compared to water, the highest increase was related to a concentration of 0.05 wt% graphene-COOH, equal to 27.8 %.

Fig. 10 illustrates the variations in the OHTC concerning the Pe at different mass concentrations of graphene-COOH nanoplates and TiO_2 NPs. As shown in Fig. 10, the OHTC increases as the Pe increases. This behavior can be explained by examining Eq. (6), which indicates that the OHTC depends on the HTR, the logarithmic temperature difference, and the cross-sectional area of heat transfer. Since the heat transfer area remains constant across all samples, the observed changes can be attributed to the other two parameters. The findings indicate that at higher Peclet numbers, the HTR increases while the logarithmic temperature difference decreases. Consequently, according to Eq. (6), these factors lead to an increase in the OHTC. As the NP concentration in the NF increases, the HTR also increases. However, this increase in the HTR is more significant, resulting in a higher OHTC than water. The maximum enhancement in OHTC related to the graphene-COOH/water NF at 0.05 wt% was 25.54 %

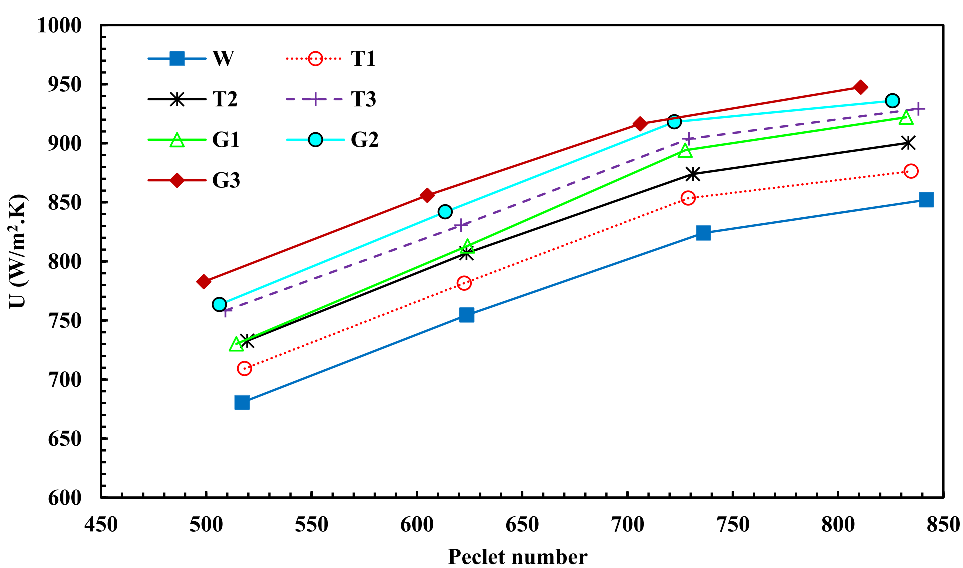

Fig. 10. Variations in the OHTC with the Pe for graphene-COOH/water and TiO_2/water nanofluids at different concentrations compared to water.

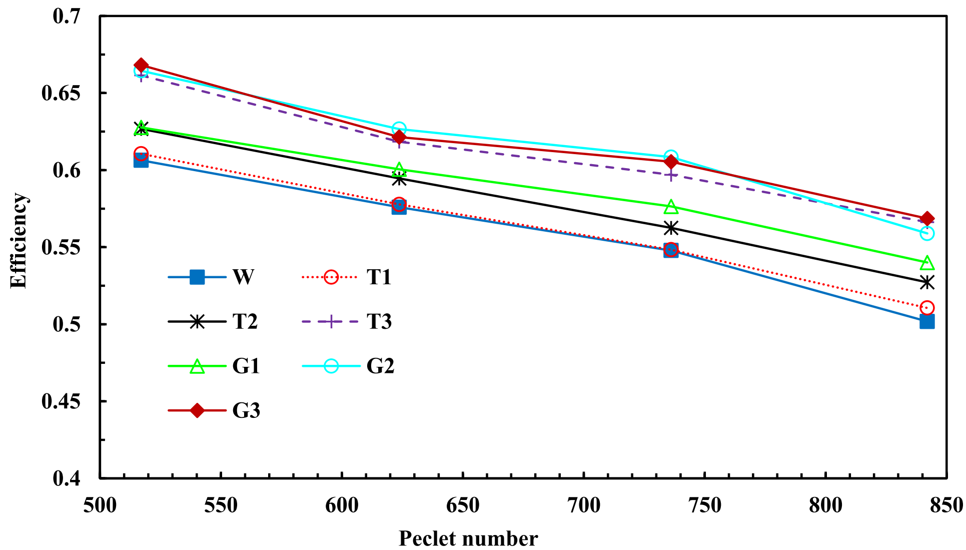

Fig. 11. Variations in the efficiency with the Pe for graphene-COOH/water and TiO_2/water nanofluids at different concentrations compared to water.

HEX efficiency was calculated using Eq. (24) and presented in terms of the Pe in three different mass concentrations of graphene-COOH nanoplates and TiO_2 NPs in Fig. 11. Based on the findings, it is evident that an increase in the Pe leads to a decrease in the HEX efficiency. In the range of the Peclet numbers from 517 to 842, the thermal efficiency value dropped from 0.6 to 0.5 for pure water. As shown in Fig. 11, an increase in flow rate leads to decrease in the HEX efficiency. This trend occurs because higher flow rates cause the fluid to pass through the HEX channels more quickly, reducing the time available for heat transfer. Consequently, the outlet temperature becomes closer to the inlet temperature, reducing the temperature difference between the HF's inlet and outlet. According to Eq. (24), this temperature difference decrease reduces the HEX efficiency. Among NFs and water, graphene-COOH/water NFs had the highest efficiency.

Table 6
The variation of friction factor and ΔP with Re_h and nanoparticle concentration.

Samples	G_h (m/s)	Re_h	Friction factor	ΔP (Pa)	$((\Delta P_{nf}-\Delta P_w)/\Delta P_w) \times 100$
W	0.027	137.1	0.34193	2020.53	–
W	0.033	158.4	0.32006	2039.20	–
W	0.038	170.2	0.30970	2063.42	–
W	0.044	193.3	0.29223	2084.34	–
T1	0.027	135	0.34432	2038.10	0.87
T1	0.033	160.4	0.31820	2054.44	0.75
T1	0.038	181.3	0.30093	2073.43	0.49
T1	0.044	203.4	0.28547	2094.16	0.47
T2	0.027	131.1	0.34895	2069.87	2.44
T2	0.033	156.8	0.32158	2086.48	2.32
T2	0.038	175.2	0.30562	2106.23	2.07
T2	0.044	204.7	0.28465	2126.05	2.00
T3	0.027	132.2	0.3476	2098.54	3.86
T3	0.033	159.1	0.31940	2115.18	3.72
T3	0.038	175.3	0.30554	2135.53	3.45
T3	0.044	190.9	0.29393	2158.28	3.55
G1	0.027	134.4	0.34499	2036.99	0.81
G1	0.033	146.3	0.33190	2055.37	0.79
G1	0.038	171	0.30827	2073.77	0.50
G1	0.044	194.5	0.29138	2094.57	0.49
G2	0.027	140.9	0.33766	2046.81	1.30
G2	0.033	154.8	0.32342	2064.76	1.25
G2	0.038	166.9	0.31251	2085.47	1.07
G2	0.044	190	0.29452	2106.35	1.05
G3	0.027	134.6	0.34481	2070.92	2.49
G3	0.033	147.2	0.33100	2089.48	2.46
G3	0.038	171.1	0.30901	2108.49	2.18
G3	0.044	187.6	0.29623	2130.84	2.23

To evaluate the ΔP and friction factor, Table 6 presents the variations in ΔP and friction factor concerning the channel mass velocity of the HF (G_h) and the Re, for graphene-COOH/water and TiO_2/water NFs at different mass concentrations of the NP additives. Based on the results, the ΔP increases with an increase in flow rate. In internal flows, an increase in fluid speed leads to a decrease in pressure, affecting the fluid pressure within the channel pathway. Additionally, it is observed that NFs exhibit slightly higher ΔP, although this difference is negligible. For example, when using a NF with graphene-COOH additives (as shown in Fig. 12), at G_h of 0.044 m/s, the relative ΔP increased slightly as the concentration rose from 0.01 wt% to 0.05 wt%, going from 1.0049 to 1.022. According to Table 6 and Fig. 12, the maximum increase in ΔP for graphene-COOH/water at 0.05 wt% was 2.49 % related to $Re_h = 134.6$, and this ΔP is negligible. For TiO_2/water NFs, as the NP concentration increased to 0.05 wt%, at $Re_h = 132.2$, the maximum increase in ΔP was 3.86 %. This was slightly higher than the increase observed for graphene-COOH/water NFs. According to Table 6, at the same Re_h, with increasing NP concentration, the friction factor slightly increased compared to water. This research used NPs at a low concentration, which had little effect on viscosity and Re. As a result, the friction coefficient did not change significantly. This is why the ΔP showed only a minor change compared to using water.

As noted, both the ΔP and the CHTC rise with increasing Reynolds numbers and greater weight concentrations. In essence, incorporating NPs into distilled water improves heat transfer, but it also leads to a higher ΔP. To analyze these conflicting effects together, it is necessary to introduce an additional parameter. Consequently, a third factor must be taken into account in conjunction with the ΔP and the heat transfer coefficient. This factor, referred to as the performance index (η), is computed using the following equation [33]:

$$\eta = \frac{\frac{h_{nf}}{h_{bf}}}{\frac{\Delta P_{nf}}{\Delta P_{bf}}} = \frac{RE_h}{RE_{\Delta P}} \tag{26}$$

RE_h represents the ratio of heat transfer enhancement when using the NF compared to water, and $RE_{\Delta P}$ denotes the ratio of the NF's ΔP to that of water. Fig. 13 shows the performance index of graphene-COOH/water and TiO_2/water NFs at different concentrations as a function of the Reynolds number. A performance index of at least 1 indicates that using the NF is beneficial. According to Fig. 13, the performance index for all the samples is greater than 1, demonstrating their practical usefulness. As shown, this index increases with both Reynolds number and weight concentration. Among the NFs, the graphene-COOH/water NF at a 0.05 wt% concentration exhibits the highest performance index, with a

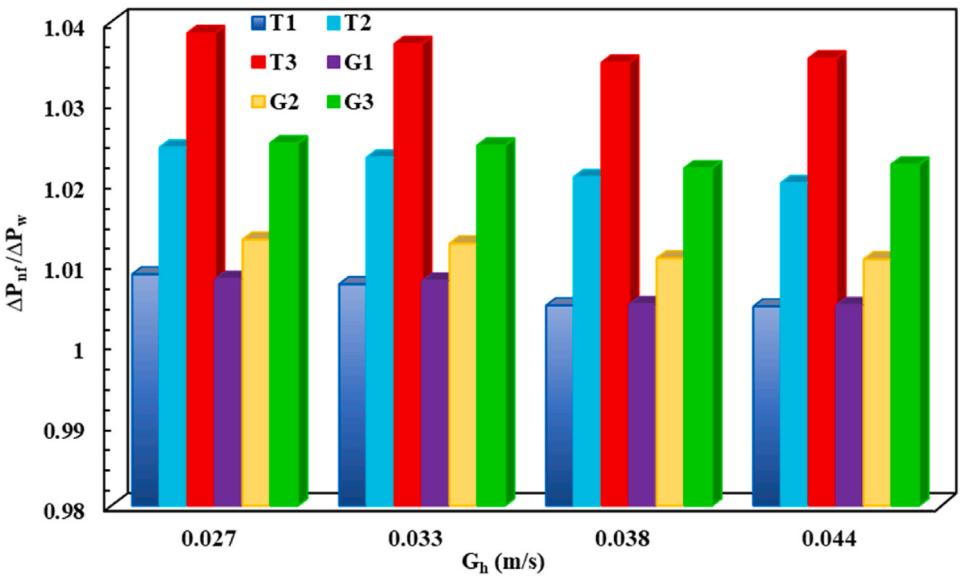

Fig. 12. Variation of ΔP with G_h for graphene-COOH/water and TiO_2/water nanofluids.

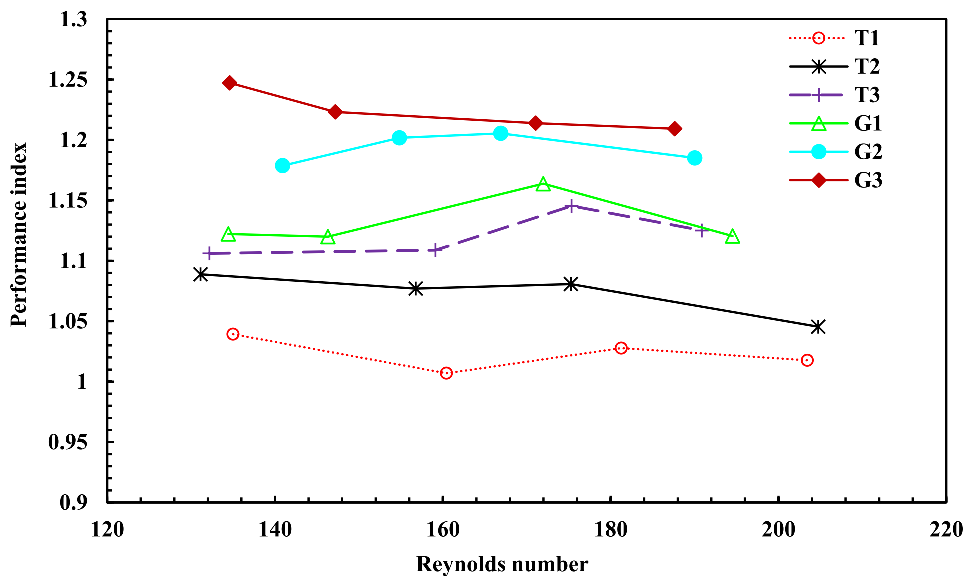

Fig. 13. Performance index of graphene-COOH/water and TiO_2/water nanofluids versus Reynolds number at different concentrations.

maximum value of 1.247 at a Reynolds number of 134.59, representing a 24.7 % increase. A higher performance index indicates that the NF surpasses the base fluid in overall effectiveness.

4. Conclusion

The initial stage involved using graphene-COOH nanoplates and TiO_2 NPs, followed by an analysis of their properties using SEM, XRD, and FTIR techniques. The stability of the NFs was assessed through zeta potential analysis. Subsequently, the effects of graphene-COOH/water and TiO_2/water NFs, with varying mass concentrations (0.01 wt%, 0.03 wt%, and 0.05 wt%), and the Pe on the CHTC, OHTC, Nu, ΔP, friction factor, and the efficiency of the PHEX were evaluated. The main findings were as follows:

1. The NF demonstrated good stability, with a zeta potential above 35.2 mV. In particular, the graphene-COOH/water NF at a mass concentration of 0.01 wt% exhibited high stability with a zeta potential of 45.5 mV. Due to its low density, graphene-COOH nanoplates tend to settle and agglomerate less in a base fluid like water compared to TiO_2 NPs.
2. With the addition of 0.05 wt% of graphene-COOH and TiO_2 to water, the TC improved by 29.6 % and 11.2 %, respectively.
3. It is well-established that using graphene-COOH/water and TiO_2/water NFs, instead of pure water, increases the CHTC and Nu. The enhancement in these two parameters indicates an augmentation in the HTR between the NFs, the wall, and, consequently, the CF. As a result, the energy recovery from the HF to the CF is amplified. The maximum enhancement in CHTC is related to graphene-COOH/water NF at 0.05 wt% was 27.8 %.
4. It was observed that the addition of both NPs at different concentrations to the base fluid resulted in a slight increase in ΔP in the channels and ducts. The maximum increase was 3.8 %, which is very negligible.

CRediT authorship contribution statement

Saeed Zeinali Heris: Validation, Supervision, Methodology, Conceptualization. **Siavash Pasvei:** Investigation, Formal analysis. **Hadi Pourpasha:** Writing – original draft, Validation, Conceptualization. **Yaghoub Mohammadfam:** Writing – original draft, Formal analysis. **Mohsen Sharifpur:** Validation. **Josua Meyer:** Validation.

Data availability

All Data generated or analyzed during this study are included in this published article.

Funding

This research did not receive any specific funding.

Declaration of competing interest

The authors declare that they have no known competing financial interests or personal relationships that could have appeared to influence the work reported in this paper.

References

[1] A. Mezaache, F. Mebarek-Oudina, H. Vaidya, Y. Fouad, Heat transfer analysis of nanofluid flow with entropy generation in a corrugated heat exchanger channel partially filled with porous medium, Heat Transfer 53 (8) (2024) 4625–4647.
[2] H.M. Maghrabie, et al., Intensification of heat exchanger performance utilizing nanofluids, Int. J. Thermofluids 10 (2021) 100071.
[3] J.J. Klemeš, et al., Heat transfer enhancement, intensification and optimisation in heat exchanger network retrofit and operation, Renew. Sustain. Energy Rev. 120 (2020) 109644.
[4] J. Zhang, X. Zhu, M.E. Mondejar, F. Haglind, A review of heat transfer enhancement techniques in plate heat exchangers, Renew. Sustain. Energy Rev. 101 (2019) 305–328.
[5] H. Pourpasha, Y. Mohammadfam, L. Khani, M. Mohammadpourfard, S.Z. Heris, Thermodynamic and thermoeconomic analyses of a new dual-loop organic Rankine–Generator absorber heat exchanger power and cooling cogeneration system, Energy Convers. Manag. 224 (2020) 113356.
[6] E.I. Jassim, F. Ahmed, Assessment of nanofluid on the performance and energy-environment interaction of Plate-Type-Heat exchanger, Therm. Sci. Eng. Prog. 25 (2021) 100988.
[7] A. Mezaache, F. Mebarek-Oudinal, H. Vaidya, K. Ramesh, Impact of nanofluids and porous structures on the thermal efficiency of wavy channel heat exchanger, Int. J. Therm. Sci. 210 (2025) 109673.
[8] V. Kumar, A.K. Tiwari, S.K. Ghosh, Application of nanofluids in plate heat exchanger: a review, Energy Convers. Manag. 105 (2015) 1017–1036.
[9] A.H. Pordanjani, S. Aghakhani, M. Afrand, B. Mahmoudi, O. Mahian, S. Wongwises, An updated review on application of nanofluids in heat exchangers for saving energy, Energy Convers. Manag. 198 (2019) 111886.
[10] F. Afshari, A. Sözen, A. Khanlari, A. Tuncer, Heat transfer enhancement of finned shell and tube heat exchanger using Fe2O3/water nanofluid, J. Cent. S. Univ. 28 (11) (2021).
[11] F. Afshari, A.D. Tuncer, A. Sözen, H.I. Variyenli, A. Khanlari, E.Y. Gürbüz, A comprehensive survey on utilization of hybrid nanofluid in plate heat exchanger with various number of plates, Int. J. Numer. Methods Heat Fluid Flow 32 (1) (2022) 241–264.
[12] F. Selimefendigil, G. Şenol, H.F. Öztop, Heat transfer enhancement in a shell and tube heat exchanger using hybrid nanofluid, in: Mathematical Modelling of Fluid Dynamics and Nanofluids, CRC Press, 2024, pp. 526–536.
[13] S. Zeinali Heris, H. Pourpasha, Y. Mohammadfam, R. Javadpoura, Y. Li, B. Su, Experimental investigation of the thermophysical and tribological properties of nano-TiO2-MnO2-doped graphene oxide/base oil ternary hybrid nanofluids, Arabian J. Sci. Eng. (2024) 1–20.
[14] H. Pourpasha, S. Zeinali Heris, R. Javadpour, M. Mohammadpourfard, Y. Li, Experimental investigation of zinc ferrite/insulation oil nanofluid natural convection heat transfer, AC dielectric breakdown voltage, and thermophysical properties, Sci. Rep. 14 (1) (2024) 20721.
[15] M. Moradgholi, S.M. Nowee, A. Farzaneh, Experimental study of using Al2O3/methanol nanofluid in a two phase closed thermosyphon (TPCT) array as a novel photovoltaic/thermal system, Sol. Energy 164 (2018) 243–250.
[16] S.Z. Heris, Y. Mohammadfam, R. Javadpour, H. Pourpasha, Nanofluids, in: Handbook of Nanomaterials, vol. 1, Elsevier, 2024, pp. 27–56.
[17] Y. Mohammadfam, S.Z. Heris, An experimental study of the influence of Fe3O4, MWCNT-Fe3O4, and Fe3O4@ MWCNT nanoparticles on the thermophysical characteristics and laminar convective heat transfer of nanofluids: a comparative study, Surf. Interfaces 43 (2023) 103506.
[18] Y. Mohammadfam, S.Z. Heris, Thermophysical characteristics and forced convective heat transfer of ternary doped magnetic nanofluids in a circular tube: an experimental study, Case Stud. Therm. Eng. 52 (2023) 103748.
[19] F. Mebarek-Oudina, I. Chabani, Review on nano-fluids applications and heat transfer enhancement techniques in different enclosures, J. Nanofluids 11 (2) (2022) 155–168.
[20] M. Basırı, H.R. Goshayeshı, I. Chaer, H. Pourpasha, S.Z. Herıs, Experimental study on heat transfer from rectangular fins in combined convection, J. Therm. Eng. 9 (6) (2023) 1632–1642.
[21] R. Barzegarian, A. Aloueyan, T. Yousefi, Thermal performance augmentation using water based Al2O3-gamma nanofluid in a horizontal shell and tube heat exchanger under forced circulation, Int. Commun. Heat Mass Tran. 86 (2017) 52–59.
[22] D. Zheng, J. Wang, Z. Chen, J. Baleta, B. Sundén, Performance analysis of a plate heat exchanger using various nanofluids, Int. J. Heat Mass Tran. 158 (2020) 119993.
[23] R. Du, D. Jiang, Y. Wang, K.W. Shah, An experimental investigation of CuO/water nanofluid heat transfer in geothermal heat exchanger, Energy Build. 227 (2020) 110402.
[24] M. Fares, A.-M. Mohammad, A.-S. Mohammed, Heat transfer analysis of a shell and tube heat exchanger operated with graphene nanofluids, Case Stud. Therm. Eng. 18 (2020) 100584.
[25] M. Bahiraei, A. Monavari, Thermohydraulic characteristics of a micro plate heat exchanger operated with nanofluid considering different nanoparticle shapes, Appl. Therm. Eng. 179 (2020) 115621.
[26] B. Jalili, N. Aghaee, P. Jalili, D.D. Ganji, Novel usage of the curved rectangular fin on the heat transfer of a double-pipe heat exchanger with a nanofluid, Case Stud. Therm. Eng. 35 (2022) 102086.
[27] A.M. Hassaan, An investigation for the performance of the using of nanofluids in shell and tube heat exchanger, Int. J. Therm. Sci. 177 (2022) 107569.
[28] A. Alklaibi, L.S. Sundar, K.V.C. Mouli, Experimental investigation on the performance of hybrid Fe3O4 coated MWCNT/Water nanofluid as a coolant of a Plate heat exchanger, Int. J. Therm. Sci. 171 (2022) 107249.
[29] W. Ajeeb, R.R.T. da Silva, S.S. Murshed, Experimental investigation of heat transfer performance of Al2O3 nanofluids in a compact plate heat exchanger, Appl. Therm. Eng. 218 (2023) 119321.
[30] B. Saleh, L.S. Sundar, Experimental study on heat transfer, friction factor, entropy and exergy efficiency analyses of a corrugated plate heat exchanger using Ni/water nanofluids, Int. J. Therm. Sci. 165 (2021) 106935.
[31] A. Hashmi, F. Tahir, U. Hameed, Empirical Nusselt number correlation for single phase flow through a plate heat exchanger, in: Proceedings of the 9th WSEAS International Conference on Heat and Mass Transfer (HMT'12), Cambridge, MA, USA, 2012, pp. 25–27.
[32] C.S. Fernandes, R.P. Dias, J.M. Nóbrega, J.M. Maia, Laminar flow in chevron-type plate heat exchangers: CFD analysis of tortuosity, shape factor and friction factor, Chem. Eng. Process: Process Intensif. 46 (9) (2007) 825–833.
[33] Z. Taghizadeh-Tabari, S.Z. Heris, M. Moradi, M. Kahani, The study on application of TiO2/water nanofluid in plate heat exchanger of milk pasteurization industries, Renew. Sustain. Energy Rev. 58 (2016) 1318–1326.
[34] S. Kakaç, H. Liu, A. Pramuanjaroenkij, Heat Exchangers: Selection, Rating, and Thermal Design, CRC press, 2002.
[35] Z.H. Ayub, Plate heat exchanger literature survey and new heat transfer and pressure drop correlations for refrigerant evaporators, Heat Transf. Eng. 24 (5) (2003) 3–16.
[36] S.B. Mousavi, H. Pourpasha, S.Z. Heris, High-temperature lubricity and physicochemical behaviors of synthesized Cu/TiO2/MnO2-doped GO nanocomposite in high-viscosity index synthetic biodegradable PAO oil, Int. Commun. Heat Mass Tran. 156 (2024) 107642.
[37] H. Pourpasha, S.Z. Heris, S.B. Mousavi, Thermal performance of novel ZnFe2O4 and TiO2-doped MWCNT nanocomposites in transformer oil, J. Mol. Liq. 394 (2024) 123727.
[38] N. Kumar, S. Das, C. Bernhard, G. Varma, Effect of graphene oxide doping on superconducting properties of bulk MgB2, Supercond. Sci. Technol. 26 (9) (2013) 095008.
[39] A.C. Ferrari, J. Robertson, Interpretation of Raman spectra of disordered and amorphous carbon, Phys. Rev. B 61 (20) (2000) 14095.
[40] Z. Wang, et al., Crystal facets controlled synthesis of graphene@ TiO 2 nanocomposites by a one-pot hydrothermal process, CrystEngComm 14 (5) (2012) 1687–1692.
[41] H. Kumar, The plate heat exchanger: construction and design, in: Institute of Chemical Engineering Symposium Series, vol. 86, Pergamon, Leeds, UK, 1984, pp. 1275–1288.
[42] D. Huang, Z. Wu, B. Sunden, Pressure drop and convective heat transfer of Al2O3/water and MWCNT/water nanofluids in a chevron plate heat exchanger, Int. J. Heat Mass Tran. 89 (2015) 620–626.
[43] M. Pantzali, A. Mouza, S. Paras, Investigating the efficacy of nanofluids as coolants in plate heat exchangers (PHE), Chem. Eng. Sci. 64 (14) (2009) 3290–3300.
[44] A. Durmuş, H. Benli, İ. Kurtbaş, H. Gül, Investigation of heat transfer and pressure drop in plate heat exchangers having different surface profiles, Int. J. Heat Mass Tran. 52 (5–6) (2009) 1451–1457.
[45] M. Gupta, V. Singh, R. Kumar, Z. Said, A review on thermophysical properties of nanofluids and heat transfer applications, Renew. Sustain. Energy Rev. 74 (2017) 638–670.
[46] K. Elsaid, et al., Thermophysical properties of graphene-based nanofluids, Int. J. Thermofluids 10 (2021) 100073.
[47] T.-H. Tsai, L.-S. Kuo, P.-H. Chen, C.-T. Yang, Effect of viscosity of base fluid on thermal conductivity of nanofluids, Appl. Phys. Lett. 93 (23) (2008).

[48] H. Pourpasha, S.Z. Heris, M. Mohammadpourfard, The effect of TiO2 doped multi-walled carbon nanotubes synthesis on the thermophysical and heat transfer properties of transformer oil: a comprehensive experimental study, Case Stud. Therm. Eng. 41 (2023) 102607.

[49] Y. Ren, H. Xie, A. Cai, Effective thermal conductivity of nanofluids containing spherical nanoparticles, J. Phys. Appl. Phys. 38 (21) (2005) 3958.

[50] R. Prasher, P.E. Phelan, P. Bhattacharya, Effect of aggregation kinetics on the thermal conductivity of nanoscale colloidal solutions (nanofluid), Nano Lett. 6 (7) (2006) 1529–1534.